CONF-8705226--1

POSITRON-ANNIHILATION 2D-ACAR STUDIES OF DISORDERED AND DEFECTED ALLOYS*

CONF-8705226--1

DE88 003118

A. Bansil and R. Prasad**
Department of Physics
Northeastern University, Boston, MA 02115

L. C. Smedskjaer and R. Benedek
Materials Science Division
Argonne National Laboratory, Argonne, IL 60439

P. E. Mijnarends
Netherlands Energy Research Foundation ECN
1755 ZG Petten, The Netherlands

September 1987

/pd

To be published in Materials Science Forum, Proceedings of the U.S.-Japan Seminar on Electronic Structure and Lattice Defects in Alloys, Honolulu, HI, May 4-8, 1987.

*Work supported by the U.S. Department of Energy, BES-Materials Sciences, under Contracts DE-FG02-85ER45223 and W-31-109-ENG-38. It benefited from the allocation of supercomputer time on the ER-Cray at the MFE computer center.

**Permanent address: Department of Physics, Indian Institute of Technology, Kanpur, India 208016.

POSITRON-ANNIHILATION 2D-ACAR STUDIES OF DISORDERED AND DEFECTED ALLOYS

A. Bansil and R. Prasad*
Department of Physics
Northeastern University, Boston Mass 02115

L. C. Smedskjaer and R. Benedek
Material Science and Technology Division
Argonne National Laboratory, Argonne, Illinois 60439

P. E. Mijnarends
Netherlands Energy Research Foundation ECN
1755 ZG Petten, The Netherlands

ABSTRACT

Theoretical and experimental progress in connection with 2D-ACAR positron annihilation studies of ordered, disordered, and defected alloys is discussed. We present, in particular, some of the recent developments concerning the electronic structure of disordered alloys, and the work in the area of annihilation from positrons trapped at vacancy-type defects in metals and alloys. The electronic structure and properties of a number of compounds are also discussed briefly; we comment specifically on high T_c ceramic superconductors, Heusler alloys, and transition-metal aluminides.

I. INTRODUCTION

Recent experimental and theoretical advances in connection with the method of angular-correlation-of-annihilation-radiation (ACAR) bring us closer to a full realization of the potential of this technique for the investigation of the electronic structure of disordered as well as defected metals and alloys. Several high-resolution, high efficiency two-dimensional angular correlation (2D-ACAR) machines are now on line in various laboratories around the world.[1-7] On the theoretical side, realistic treatment of electron as well as electron-positron momentum densities relevant for Compton scattering and positron annihilation in

* Permanent address: Department of Physics, Indian Institute of Technology, Kanpur, India 208016

disordered alloys has become possible.[8-13] A similarly sophisticated treatment of vacancy-type defects in metals and alloys can be anticipated. The increasing availability of high-speed computers should permit extension and application of these theoretical techniques to more complex systems.

This article focusses on recent developments in three specific areas, namely, disordered alloys, vacancy-type defects in metals and alloys and, finally, work on some ordered compounds. In the spirit of the discussions at the US/Japan Workshop, our aim is to give the reader an overview of the present status of the field and, when appropriate, an indication of what we believe to be some of the more interesting areas of ongoing and future research activity. The examples presented are mostly taken from the work of the present group of authors. The citation of literature, while not very extensive, is representative.

An outline of this article is as follows. After the introductory remarks of Section I, we consider disordered alloys in Section II. The basic equations for evaluating the configurationally averaged electron momentum density, $\rho(\vec{p})$, and the electron-positron momentum density, $\rho_{2\gamma}(\vec{p})$, within the framework of the modern KKR-CPA- based band theory of alloys[8-13] are stated. Illustrative results for $CuNi$ alloys are presented. Recent results which compare the 2D-ACAR measurements on disordered $CuGe$[14] and $CuPd$[15] alloy single crystals with corresponding KKR-CPA momentum density computations are described.

Section III turns to positron annihilation from vacancy-type defects in metals and alloys. The positron state in the preceding consideration of annihilation from alloys is Bloch-like and thus extended. In contrast, as is well known, positrons have a tendency to trap at vacancy-type defects in materials; see references 16-18 for recent reviews concerning defect-related work. This case differs fundamentally from the Bloch- state case because for the trapped positron, it is most natural to carry through the formalism in real space rather than in momentum space. The relevant formalism for annihilation from a mono-vacancy, a di-vacancy, and from other small defects such as vacancy-impurity complexes is outlined.[19] Results of the application of the theory to the case of a mono-vacancy in Cu, the first such calculations for a d-band metal, are presented as an example. The 2D-ACAR experiments , combined with $\rho_{2\gamma}(\vec{p})$ calculations , should provide a defect-specific probe of vacancy-type defects in metals and alloys.

Section IV considers ordered compounds. We comment on systems of current interest to the present group of authors; these include high-T_c ceramic superconductors, heavy-Fermion alloys, Heusler alloys, and advanced alloys, especially the Fe and Ni aluminides, which are important high-temperature intermetallics; experimental and theoretical work is currently in progress in all these cases. Some of the difficulties encountered in the theoretical consideration of momentum densities in such complex systems are stated.

In conclusion, we believe that 2D-ACAR experiments on ordered and disordered alloys, with or without defects, together with theoretical momentum density computations, should provide interesting new insights into the electronic structure and properties of a wide range of materials.

II. DISORDERED ALLOYS

IIA. Electron Momentum Density

The quantity of central interest for discussing the electron momentum density $\rho(\vec{p})$ is the $(\vec{p},\vec{p})$ matrix element of the electron Green's function, in terms of which $\rho(\vec{p})$ is expressed as [20]

$$\rho(\vec{p}) = -\frac{1}{\pi}\int_{-\infty}^{E_F} dE\, Im\, < G(\vec{p},\vec{p};E) > \tag{1}$$

$$= \int_{-\infty}^{E_F} dE\, \rho(\vec{p},E). \tag{2}$$

where $\rho(\vec{p},E) \equiv -\pi^{-1} Im < G(\vec{p},\vec{p};E) >$ is the spectral momentum density.

Equation 1 is a convenient starting point for the calculation of average momentum density in alloys because $< G >$ can be calculated within the framework of the CPA or the ATA theory. In particular, for a general ordered medium of effective atoms, $\rho(\vec{p},E)$ is expressed in terms of atomic quantities as[20]

$$\rho(\vec{p},E) = -\frac{1}{\pi} Im[\frac{1}{E+i0^+-p^2} + \frac{(4\pi)^2 N}{(E+i0^+-p^2)^2}\sum_{LL'} Y_L(\hat{p})[F_1+F_2]_{LL'}Y_{L'}(\hat{p})], \tag{3}$$

where

$$F_1^{LL'} = [t_l(p,p) - \frac{t_l(p,\kappa)t_l(\kappa,p)}{t_l(\kappa,\kappa)}]\,\delta_{LL'}, \tag{4a}$$

and

$$F_2^{LL'} = \frac{t_l(p,\kappa)}{t_l(\kappa,\kappa)}[t_l(\kappa,\kappa)^{-1} - B(\vec{k},E)]^{-1}_{LL'}\frac{t_{l'}(\kappa,p)}{t_{l'}(\kappa,\kappa)}. \tag{4b}$$

Here, $\kappa \equiv \sqrt{E}$, N is the number of atoms/unit volume, $L \equiv (l,m)$ is a composite angular momentum index and Y_L the corresponding spherical harmonic, $t_l(p,p')$ are the general matrix elements of the effective medium t-matrix, and B($\vec{k}$,E) is the matrix of the KKR structure constants.

Equations 1-4 yield the ATA or the CPA momentum density depending on the specific form of the t-matrix. For a random binary alloy A_xB_{1-x}, the ATA corresponds to the choice

$$t_{ATA}(\vec{p},\vec{p}') = < t(\vec{p},\vec{p}') > \equiv x\, t_A(\vec{p},\vec{p}') + (1-x)\, t_B(\vec{p},\vec{p}'), \tag{5}$$

where t_A and t_B are the A and B atom t-matrices. The CPA scatterer is defined by the

matrix equation

$$t_{CPA}(p,p') = < t(p,p') > -[t_A(p,\kappa) - t_{CPA}(p,\kappa)]\, F_{CPA}(E)\, [t_B(\kappa,p') - t_{CPA}(\kappa,p')], \quad (6)$$

where

$$F_{CPA}(E) \equiv \frac{1}{N} \sum_{\vec{k}} B_{\vec{k}} (1 - \tau_{CPA} B_{\vec{k}})^{-1}. \quad (7)$$

Here, $\tau \equiv t(\kappa,\kappa)$ denotes the on-the-energy-shell elements of the t-matrix; these elements are more familiar than the off-the-energy-shell elements $t(p,p')$ for p and/or $p' \neq \kappa$. The summation in equation 7 extends over the Brillouin zone. Note that for $p = p' = \kappa$, equation 6 is a complicated condition for evaluating the quantities $\tau_{CPA}(E)$. In contrast, for the half- off-shell elements (i.e. $t(p,\kappa)$ and $t(\kappa,p)$ for $p \neq \kappa$) equation 6 is linear in the unknowns. In fact, once τ_{CPA} is obtained, all other elements of the CPA t-matrix are straightforwardly computed in terms of τ_{CPA} without the need to solve any additional non-linear equations.

The nature of the spectral density given by equations 3 and 4 deserves some comment even in this brief survey. The free electron poles present in the first and the second terms on the right side of equation 3 can be shown to cancel exactly so that $\rho(\vec{p},E)$ varies smoothly near $E = p^2$. The important structure in $\rho(\vec{p},E)$ arises from the presence of the inverse matrix in equation 4(b) and is thus controlled by the secular equation

$$\| \tau^{-1}(E) - B(\vec{k},E) \| = 0. \quad (8)$$

In the perfect crystal limit equation 8 gives the band structure in the KKR scheme. This equation therefore forms a natural basis for generalizing the concept of Bloch energy bands to disordered alloys. Predictions of the alloy theory in this respect have been tested via angle-resolved photoemission spectroscopy and a wide ranging agreement between theory and experiment has been found to exist in $\vec{k}$-point-by-$\vec{k}$-point detail in the various cases studied.[13,21]

IIB. Electron-Positron Momentum Density

The average momentum density $\rho_{2\gamma}(\vec{p})$ relevant for the angular correlation of (two-photon) annihilation radiation in a disordered alloy can be expressed in terms of the electron and positron Green's functions as[22]

$$\rho_{2\gamma}(\vec{p}) = \frac{1}{\pi^2} \int d\vec{r} \int d\vec{r}\,' exp[-i\vec{p}\cdot(\vec{r}-\vec{r}\,')] \int dE\, f(E) \int dE_+\, f_+(E_+) \times < Im\, G(\vec{r},\vec{r}\,';E)\; Im\, G_+(\vec{r},\vec{r}\,';E_+) >, \quad (9)$$

where + refers to the positron quantities and $f(E)$ is the Fermi-Dirac distribution function. In the spirit of the independent-particle model(IPM), it is reasonable to decouple the

average of $< ImG\ ImG_+ >$ as

$$< ImG\ ImG_+ > \longrightarrow Im < G > \ Im < G_+ > \qquad (10)$$

Form (10) is expected to be a good approximation in transition and noble metal alloys. Use of the convolution theorem on the right side of equation 9 then yields

$$\rho_{2\gamma}(\vec{p}) = \frac{1}{\pi^2} \sum_{\vec{k}+} \int dE f(E) \int dE_+ f_+(E_+) \sum_{nn'} < ImG(\vec{p} - \vec{k}_+ - \vec{K}_n, \vec{p} - \vec{k}_+ - \vec{K}_{n'}; E) >$$
$$\times < ImG_+(\vec{k}_+ + \vec{K}_n, \vec{k}_+ + \vec{K}_{n'}; E_+) >. \qquad (11)$$

By comparing forms 3 and 11, it will be seen that the evaluation of $\rho(\vec{p})$ only requires the diagonal elements $Im < G(\vec{p}, \vec{p}) >$, but to compute $\rho_{2\gamma}(\vec{p})$ a knowledge of the general elements $Im < G(\vec{p}, \vec{q}) >$ and $Im < G_+(\vec{p}, \vec{q}) >$ is required. These quantities can be obtained via a straightforward generalization of form 3 for the electrons as well as the positron; care is however necessary in the positron case since only the properties of states near the positron band edge in the alloy are involved.

Effects of electron-positron correlations, neglected in writing equations 9 and 11, should be included in a proper theory of $\rho_{2\gamma}(\vec{p})$. The semi-empirical "momentum" as well as "energy" and angular-momentum dependent enhancement schemes[23-24] of the sort that have been invoked by various authors in perfect metals should not be difficult to adapt to the case of alloys. The problem of self-consistency should be formulated within the framework of a two-component density functional theory[25-27]. More work is necessary in this regard because little experience exists at this time in treating such enhancement effects for alloys.

Figures 1 and 2 provide illustrative $\rho(\vec{p})$ and $\rho_{2\gamma}(\vec{p})$ results in CuNi solid solutions.[22] The upper set of curves in figure 1 shows that some of the changes in $\rho(\vec{p})$ as we go from Ni to Cu are: (i) the break at approximately 0.5 a.u. in Ni in the first Brillouin zone(BZ) moves to higher momenta on alloying and the size of the break increases; this results from an increase in the [110] Fermi Surface(FS) radius k_{110} and of the s-p character of the associated states with increasing Cu concentration . (ii) The [110] FS radius also yields "Umklapp" breaks in $\rho(\vec{p})$ around p= 2 a.u.; these breaks move to correspondingly lower momenta with increasing k_{110}. (iii) In the alloys the breaks are not sharp but are rounded due to disorder scattering of electrons. The preceding changes are seen to persist qualitatively in the lower set of curves for $\rho_{2\gamma}(\vec{p})$. However, the $\rho_{2\gamma}(\vec{p})$ curves decrease more rapidly with p compared to $\rho(\vec{p})$ and thus appear to be more peaked in the first BZ. This difference between $\rho(\vec{p})$ and $\rho_{2\gamma}(\vec{p})$, which occurs more generally, is a consequence of the nuclear repulsion of the positron.

Figure 2 considers the momentum density along an off-the-zone-center direction. The particular direction shown is interesting because a dip is seen around $p_z = 1.8$ a.u. in Ni and $Cu_{25}Ni_{75}$ but not in Cu or $Cu_{50}Ni_{50}$; this dip arises from the presence of d-hole pockets in the Ni-rich alloys. It turns out that, due to momentum and angular momentum

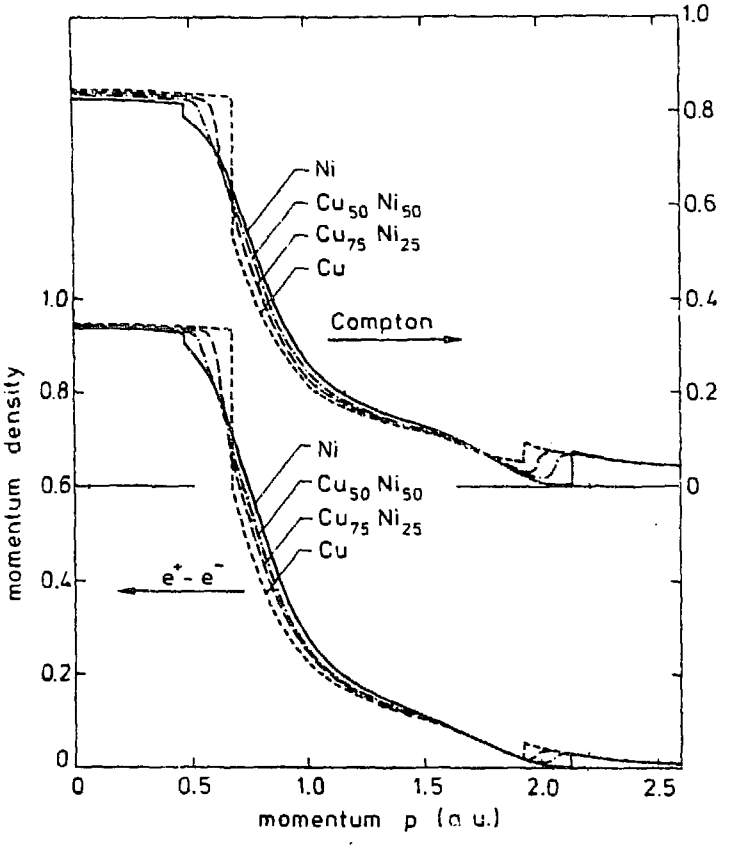

FIGURE 1: Electron momentum density $\rho(\vec{p})$ (upper set of curves) and electron-positron momentum density $\rho_{2\gamma}(\vec{p})$ (lower set of curves) in Cu, $Cu_{75}Ni_{25}$, $Cu_{50}Ni_{50}$, and Ni along the [110] direction. [After Ref. 22].

selection rules, the disappearance/appearance of d-holes does not cause a dramatic change in the momentum density in the first BZ, but larger effects occur along the off-center direction at higher momenta in figure 2. By comparing the upper and lower set of curves, we further note that this dip continues to be seen clearly even when the positron spatial distribution effects are included, although the size of the dip is reduced.

The experiments usually do not measure the three-dimensional functions $\rho(\vec{p})$ and $\rho_{2\gamma}(\vec{p})$ but only their one or two dimensional integrals in the momentum space. In this connection, figure 3 considers the Compton profile $J(q)$ in $CuNi$ alloys[28] which for a polycrystal is given by

$$J(q) = 2\pi \int_q^\infty dp\, p < \rho(\vec{p}) >_{dir}, \tag{12}$$

where the brackets denote an angular average in $\vec{p}$ space. In the calculations of figure 3 the angular average was carried out by using one special direction[29]. The agreement

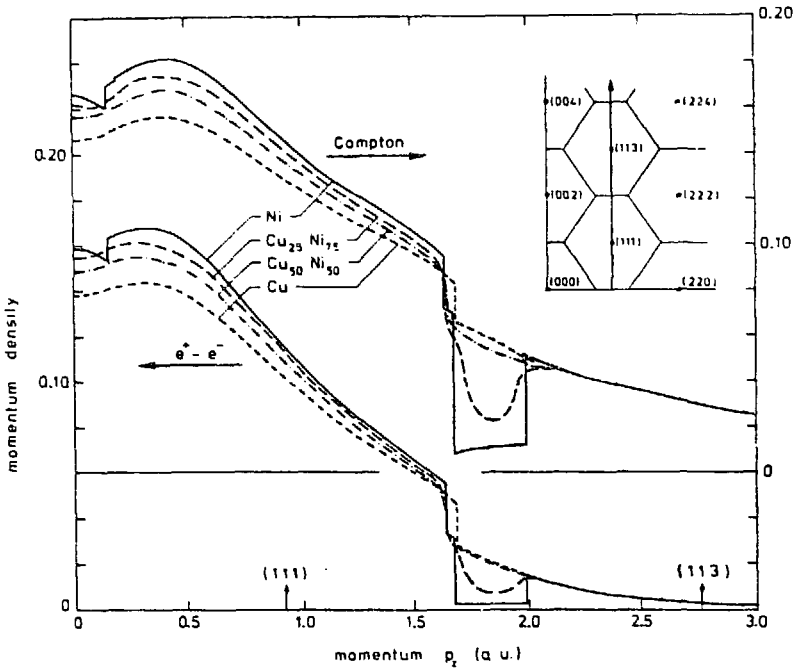

FIGURE 2: Same as the caption to figure 1, except that this figure gives momentum densities along the off-the-zone-center direction joining the (111) and (113) reciprocal lattice points (see inset).[After Ref. 22].

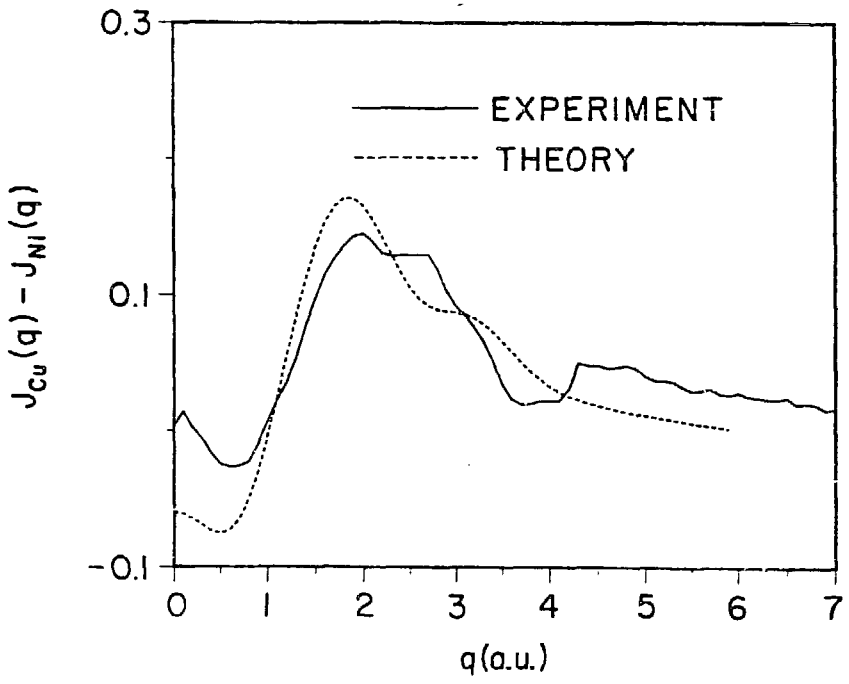

FIGURE 3: Measured and calculated difference $[J_{Cu}(q) - J_{Ni}(q)]$ between the Cu and Ni Compton profiles.[After Ref. 28].

for $J_{Cu} - J_{Ni}$ between theory and experiment is seen to be good, despite the fact that $|J_{Cu} - J_{Ni}|$ is at most a few percent of the value of $J_{Cu}(q)$. Both curves in the figure show a minimum at $p \approx 0.6$ a.u. This feature is associated with the condition $\rho_{Cu}(p) = \rho_{Ni}(p)$ which indeed occurs around a p value of 0.6 a.u. in $CuNi$ alloys close to the FS break in Cu in the first BZ (see, e. g., figure 1); the maximum at $p \approx 2$ a.u. posseses the same physical origin and it reflects the position of the FS break in the fourth BZ. The broad dip around p=4 a.u. in the solid curve is an artifact of the experiments and is not physically important; it has to do with the K-electron contribution which due to experimental conditions is included in the spectra in the range of 3.3-4.3 a.u. only in $J_{Ni}(q)$ but not in $J_{Cu}(q)$. Reference 28 further compares KKR-CPA calculations with Compton measurements on CuNi alloys and finds a good overall agreement for the entire range of compositions. These results suggest that it may be possible to extract useful information concerning FS geometry from high-resolution Compton experiments on alloys, especially if single crystals are used.

IIC. Recent Results in CuGe and CuPd Solid Solutions

We have recently carried out extensive 2D-ACAR measurements in $\alpha - Cu_{91}Ge_9$[14] and in $CuPd$[15] solid solutions containing up to 25% Pd, together with corresponding KKR-CPA calculation based on the electron momentum density $\rho(\vec{p})$. We divide our comments as follows.

IIC.1 2D-ACAR Spectra and Electron States at the Valence Band Edge

Figures 4 and 5 show that very substantial changes occur in $\rho(\vec{p})$ as Cu is alloyed with Ge or Pd. $\rho(\vec{p})$ in Cu is flat and featureless in the first BZ, but in CuGe it develops a pronounced peak and in CuPd a dip at $\vec{p} = 0$. These effects contrast sharply from the case of CuNi alloys discussed in Figure 1 where the momentum density remains quite flat in the first BZ. Due to momentum and angular momentum selection rules, $\rho(\vec{p})$ at $\vec{p} = 0$ arises from states around the valence band edge; in particular, the d-bands do not contribute to $\rho(\vec{p})$ at $\vec{p} = 0$. The electron states at the valence band edge, which lie some 10 eV below the Fermi energy E_F are not accessible in any other experiment; in photoemission, for example, these states possess rather small intensities and are masked by background and secondary emissions. CuGe and CuPd thus provide the first examples where alloying effects deep in the spectrum produce clear signatures in $\rho(\vec{p})$.

We discuss now the 2D-ACAR spectra in CuGe and CuPd and the extent to which these spectra reflect the behavior of $\rho(\vec{p})$ near $\vec{p} = 0$. After taking the instrumental response into account, the 2D-ACAR distribution is given by an integration of $\rho_{2\gamma}(\vec{p})$ along the detector axis:

$$N(p_y, p_z) \propto \int dp_x \, \rho_{2\gamma}(\vec{p}). \tag{13}$$

The theoretical 2D-ACAR results of figures 6 and 7 are based on the use of $\rho(\vec{p})$ rather than $\rho_{2\gamma}(\vec{p})$; this approximation amounts to the neglect of positron spatial distribution effects in computing $\rho_{2\gamma}(\vec{p})$ but it is not important for the present purpose of investigating

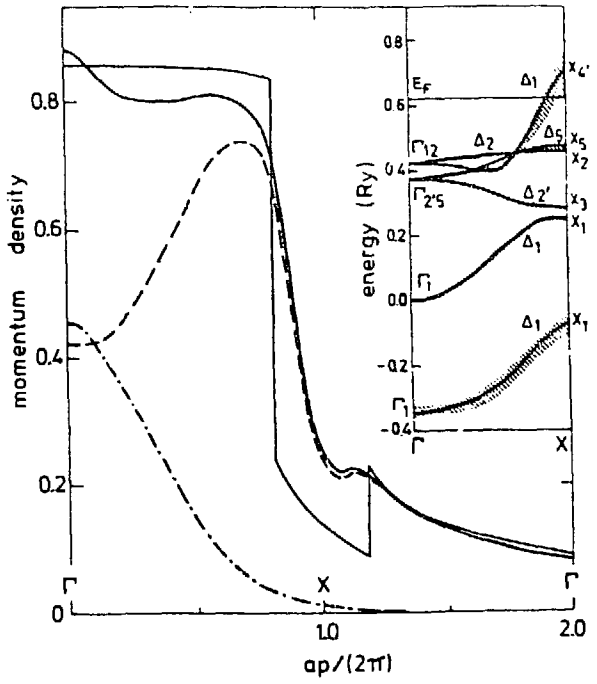

FIGURE 4: $\rho(\vec{p})$ along [100] in Cu (thin solid curve) and $Cu_{90}Ge_{10}$ (heavy solid curve). Contributions to $\rho(\vec{p})$ in the alloy for $E \geq 0$ (dashed) and $E < 0$ (chain curve) are shown. The inset gives complex band structure of $Cu_{90}Ge_{10}$ after reference 30.

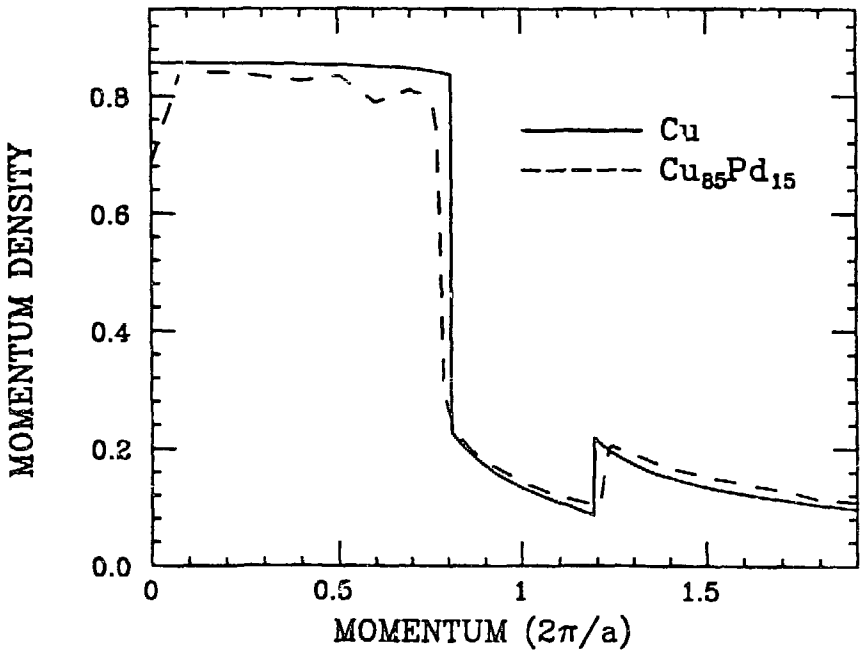

FIGURE 5: $\rho(\vec{p})$ in Cu (solid) and $Cu_{85}Pd_{15}$ (dashed) along the [100] direction.[After Ref. 15].

the behavior of the momentum density near $\vec{p} = 0$. [Figure 1 shows, for example, that $\rho(\vec{p})$ and $\rho_{2\gamma}(\vec{p})$ possess a very similar shape near $\vec{p} = 0$; the proper inclusion of the positron mainly reduces the high momentum components of $\rho(\vec{p})$.]

A bump near $\vec{p} = 0$ is seen to appear from figure 6 in the theoretical (thin solid) as well as the experimental derivative spectra (dashed) in CuGe; this bump is not present in Cu. A calculation in which the p_x integration in equation 13 is restricted artificially to the range -1/2 to 1/2 (in units of $2\pi/a$) rather than the range $-\infty$ to $+\infty$ produces an essentially identical bump in CuGe but a practically zero derivative in Cu. It is clear then that the bump in the CuGe derivative spectra arises from the peak in $\rho(\vec{p})$ near $\vec{p} = 0$ and constitutes a signature of the states at the valence band edge in the 2D-ACAR spectrum. The complex energy bands in CuGe differ fundamentally from Cu; in particular, the Cu-rich CuGe alloys possess a new Ge-derived impurity band of s-p character (the lower Δ_1 band in the inset in figure 4). The agreement between theory and experiment in figure 6 offers evidence for the existence of this Ge-derived band in the alloy and a confirmation of the KKR-CPA predictions[30] in this regard.

Figure 7 compares cuts through the 2D-ACAR measurements in CuPd alloys with the associated theoretical curves. A distinct flattening of the experimental curves near $\vec{p} = 0$ is evident. This feature, which is reproduced in the calculations, arises substantially from the dip in $\rho(\vec{p})$ near $\vec{p} = 0$ discussed in connection with figure 5 above. These results, like those on CuGe, indicate that 2D-ACAR experiments can yield information concerning rather subtle features of the electronic spectrum if they are used in parallel with corresponding theoretical work.

IIC.2 Fermi Surface

In this connection, we return to figure 6. The Cu derivative spectrum (upper set of points) shows a peak at $p_y \approx 5.4$ mrad and a dip at ≈ 8.1 mrad; these features arise from FS breaks in $\rho(\vec{p})$. Upon alloying, both features are considerably smoothed, the former moves to a higher and the latter to a lower momentum (lower set of points). These effects are qualitatively expected because on adding Ge the FS of Cu expands and becomes smeared due to disorder scattering of states.

The FS radii are in principle given by the positions of extrema in the 2D-ACAR derivative spectra. The finite instrumental resolution, however, can shift the positions of the extrema and in general a more detailed analysis is necessary. In reference 14 the FS radii k_{100} and k_{110} , together with the associated dampings, were obtained from the experimental derivative spectra by using model calculations employing an anisotropic parabolic conduction band with dispersion relation

$$E_{\vec{k}} = k^2[C_0 + C_4(k_x^4 + k_y^4 + k_z^4) + C_6 k_x^2 k_y^2 k_z^2 + C_8(k_x^8 + k_y^8 + k_z^8)], \qquad (14)$$

where k_x, k_y, k_z are the direction cosines of the wave vector $\vec{k}$. The constants C_0, C_4, C_6, and C_8 describe the shape of the FS and were determined by fitting the FS to the Halse-Cu7[31] FS in the angular region of interest. A model momentum density based on equation 14

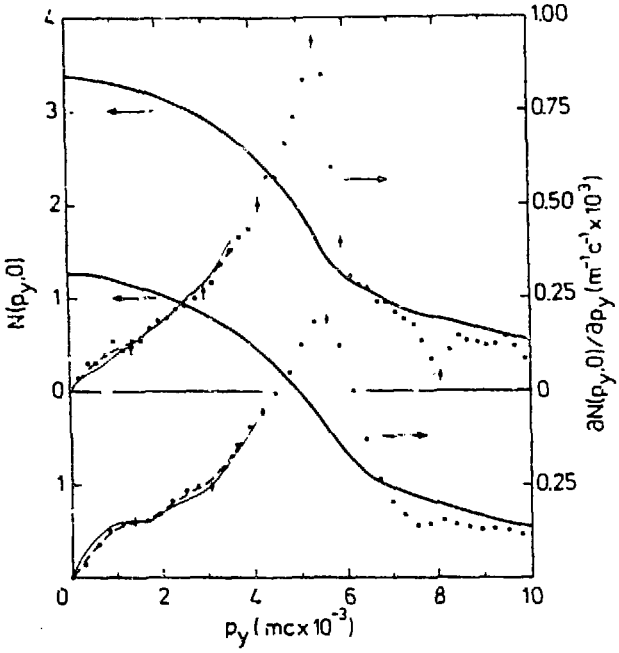

FIGURE 6: Cuts along $p_y = [010]$ through the 2D-ACAR distribution (solid lines) with $p_x = [100]$ in Cu (top) and $Cu_{91}Ge_9$ (bottom). The dots give the experimental derivatives. In the low p-region the theoretical derivative (thin solid) and the more heavily smoothed experimental derivatives are shown.[After Ref. 14].

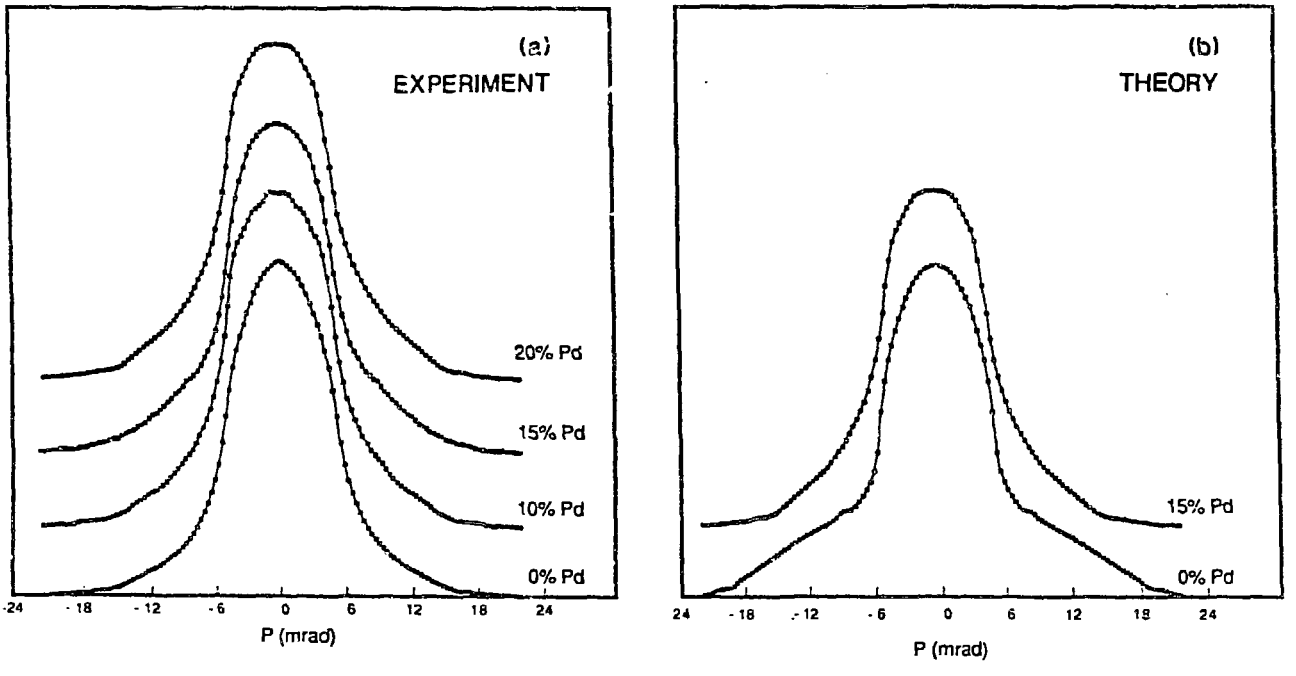

FIGURE 7: Experimental (a) and theoretical (b) [100] cuts of the [001] 2D-ACAR surface for $CuPd$ alloys.[After Ref. 15].

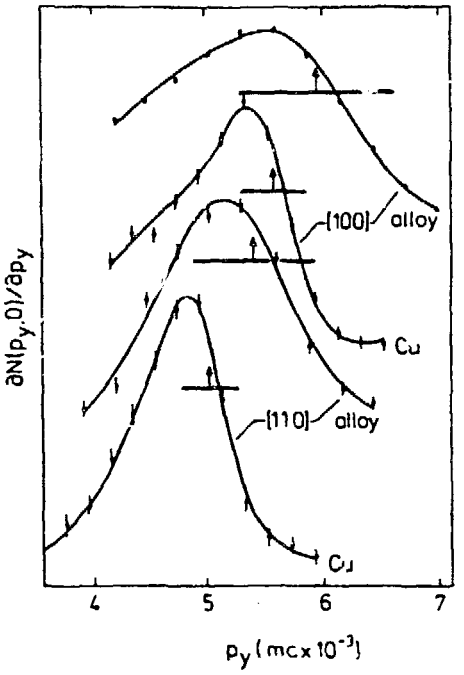

FIGURE 8: Derivatives $dN(p_y,0)/dp_y$ (in a limited range around k_F) for $(p_y,p_z) = ([010],[001])$ and $([110],[001])$. The curves give fits of the model described in the text. Arrows indicate the fitted Fermi surface radii, heavy lines represent the smearing $2\Delta k_F$. [After Ref. 14].

was then obtained by giving a Lorentzian line broadening to all occupied levels; this model has the advantage that an analytic solution for $\rho(\vec{p})$ is possible. After convolution with the instrumental resolution function, the model $N(p_y,0)$ was differentiated and fitted to the measurements over the range $0.75k_F < p_y < 1.2k_F$. Figure 8 shows that the fits are excellent in all cases considered.

Table I summarizes the FS results in Cu and $Cu_{91}Ge_9$. It should be emphasized that the high precision in determining k_{100} and k_{110} in 2D-ACAR measurements was made possible by the use of *a priori* knowledge of the shape of the Cu FS. The measured FS radii in $Cu_{91}Ge_9$ are in good accord with the KKR-CPA predictions. The measured dampings Δk_F are approximately 50% larger than the theoretical values. The overall agreement between the KKR-CPA values and the measurements is to be considered satisfactory in view of inherent uncertainties in the first principles electronic structure calculations.

We turn now to the discussion of 2D-ACAR determination of FS radii in CuPd alloys. In order to extract the FS radii, as in the case of CuGe discussed above, a proper analysis of the 2D-ACAR data is necessary. In this connection, reference 15 focusses on the question of possible flattening of the FS of Cu along the [110] direction upon adding Pd. KKR-CPA calculations predict an appreciable flattening effect up to about 40 *at*% Pd.[32-34] This flattening is believed to be responsible for driving the short-range order that has been

TABLE I. Fermi radii and associated disorder smearings along [100] and [110] directions in Cu and $Cu_{91}Ge_9$. Δk_F denotes 1/2 of the full width of the smearing function. All quantities in mrad units; 1 mrad= 2.5896 nm^{-1}.

	Cu		$Cu_{91}Ge_9$	
	2D-ACAR (Ref. 14)	dHvA (Ref. 31)	2D-ACAR (Ref. 14)	KKR-CPA (Ref. 30)
k_{100}	5.58±0.02	5.58±0.01	5.94±0.10	5.93
k_{110}	5.03±0.02	5.01±0.01	5.42±0.03	5.32
Δk_{100}	....	....	0.5±0.1	0.35
Δk_{110}	....	....	0.4±0.1	0.23

observed in CuPd alloys in diffuse electron and x-ray scattering studies.[35-36] Note that an analysis in the present case along the lines of the preceding CuGe data would not be meaningful; in CuGe the shape of the FS was assumed to be same in Cu and the alloy, the focus was on determining the FS smearing; in CuPd, the FS smearing is rather small and the main purpose was to determine changes in the FS shape on alloying.

With these remarks in mind, the [100] FS radius k_F was determined in reference 15 by fitting the 2D-ACAR CuPd data to a model spectrum parametrized in terms of elliptical and Gaussian terms:

$$N(p_x, p_y) = I_1 E(p_x, p_y) + I_2 G(p_x, p_y), \tag{15}$$

where

$$E(p_x, p_y) = \begin{cases} [1 - (p_x/k_F)^2 - (p_y/k_t)^2]^{1/2}, & \text{for } (p_x/k_F)^2 + (p_y/k_t)^2 < 1; \\ 0, & \text{otherwise,} \end{cases} \tag{16}$$

and

$$G(p_x, p_y) = exp\{-1/2[(p_x/\sigma_F)^2 + (p_y/\sigma_t)^2]\}. \tag{17}$$

Least-squares fits of the parameters $I_1, I_2, \sigma_F, \sigma_t, k_t$, and k_F were made, taking the instrumental resolution into account. The [110] radius was not analyzed in reference 15 via equations 15-17 because for the experimental geometry (i.e. [100] integration direction in equation 13) the FS of Cu near [110] in the first BZ overlaps with the projected FS in the second BZ as well as with the projection of the FS necks, making the underlying assumptions of the model unreasonable. Nevertheless, it was possible to obtain a reasonably accurate value of the [110] radius from the peak positions in the derivative spectra, despite a fairly complicated FS geometry. The results for k_{100} and k_{110} are summarized in figure 9. The estimated error in the determination of the FS radii are ± 0.04 mrad and ± 0.08 mrad for the [100] and [110] radius respectively.

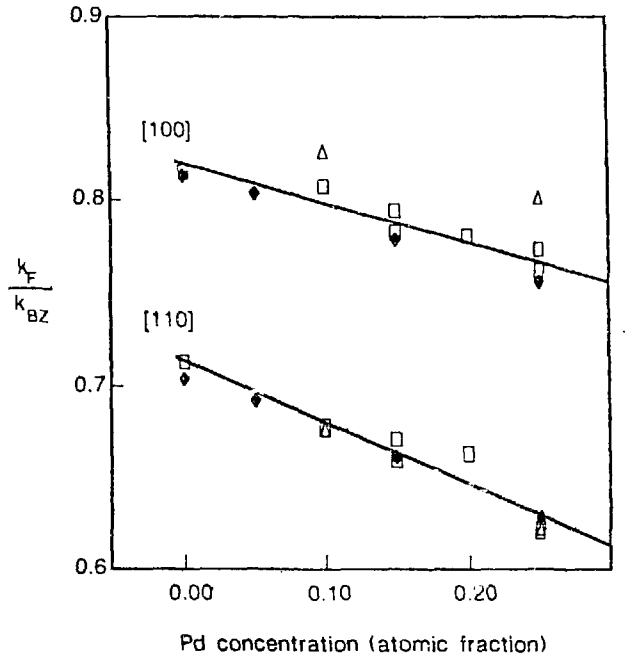

FIGURE 9: k_F/k_{BZ} where k_F is the FS radius in a given direction and k_{BZ} is the Brillouin zone dimension in the same direction. Radii along [100] and [110] direction are shown. Least squares fits through the data of Ref. 15 (open squares) are shown by solid lines. Theoretical results are: reference 33 (filled diamonds), and reference 32 (open triangles).

The agreement between theory and experiment in figure 9 is excellent, especially with the KKR-CPA calculations of reference 33. The more rapid decrease of k_F/k_{BZ} in the [110] direction compared to the [100] direction provides clear evidence that the FS of Cu indeed flattens along [110] upon alloying. We note that this flattening effect is seen in KKR-CPA calculations in other Cu-based alloys with decreasing electron/atom ratio as well as in the rigid band computations.[10] The present 2D-ACAR results differ substantially from the lower-resolution point slit angular-correlation experiments of Hasegawa *et. al.*[37]; in particular, the slope of the k_{110} line (lower solid) in figure 9 is 60% greater than that of a straight line drawn through the data of reference 37; the present k_{110} slope is in fact in good accord with the values deduced by Ohshima and Watanabe[35] from diffuse electron scattering.

So far we have focussed primarily on the behavior of $\rho(\vec{p})$ near $\vec{p} = 0$ and the FS breaks. But figures 6 and 7 show many other changes in the 2D-ACAR spectra of Cu upon alloying; see, for example, the region $p > 6$ mrad in the figures. To understand these effects a full computation of the $\rho_{2\gamma}(\vec{p})$ along the lines of equation 11 is necessary. Studies of other alloys, magnetic as well as non-magnetic, in the spirit of the present approach should prove worthwhile.

III. VACANCY- TYPE DEFECTS IN METALS AND ALLOYS

IIIA. Formalism: Annihilation from a Trapped Positron

It is convenient to cast the general equation 9 in the form[19]

$$\rho_{2\gamma}(\vec{p}) = \sum_{mn} M_{mn}(\vec{p})\, e^{i\vec{p}\cdot(\vec{R}_m - \vec{R}_n)}, \tag{18}$$

where $\{\vec{R}_m\}$ is the set of lattice vectors. [Reference 34 considers representation 18 for $\rho_{2\gamma}(\vec{p})$ for Bloch-state positron in disordered alloys.] By using the expansion[38,39]

$$Im\, G(\vec{r}_1, \vec{r}_2, E) = \sum_{LL'} Z_L^m(\vec{r}_1 - \vec{R}_m, E)\; Im\, T_{LL'}^{mn}\; Z_{L'}^{(n)}(\vec{r}_2 - \vec{R}_n, E), \tag{19}$$

where $\vec{r}_1(\vec{r}_2)$ lies in the Wigner Seitz cell on the $m(n)$ site, $Z_L^{(i)}$ is the regular solution of the Schrödinger equation in the i^{th} muffin-tin sphere, and

$$T(E) = [\tau^{-1} - B(E)]^{-1} \tag{20}$$

is the path operator matrix in the site indices n and the angular momenta L. B is similarly a matrix which in a perfect crystal is the Fourier transform of the KKR structure constant matrix encountered in equation 4(b) above. By using expansion 19 for the electron as well as the positron Green's function, the coefficient M_{mn} can be written as[19]

$$M_{mn}^{\alpha\beta}(\vec{p}) = \frac{1}{\pi^2} \int dE f(E) \int dE_+ f(E_+) \sum_{L_1 L_1'} \sum_{L_2 L_2'} \Delta_{L_1 L_2}^{m\alpha}(\vec{p}, E, E_+)$$
$$\times \Delta_{L_1' L_2'}^{n\beta}(-\vec{p}, E, E_+)[Im\, T_{L_1 L_1'}^{e,mn}(E)\, Im\, T_{L_2 L_2'}^{p,mn}(E_+)], \tag{21}$$

where

$$\Delta_{LL'}^{i\alpha}(\vec{p}, E, E_+) = 4\pi \sum_{L''} (-i)^{l''} Y_{L''}(\hat{p}) \int_{\Omega_i} d^3r\, Z_L^{e,i\alpha}(\vec{r}, E) Z_{L'}^{p,i\alpha}(\vec{r}, E_+) Y_{L''}(\hat{r})\, j_{l''}(pr). \tag{22}$$

The superscript $\alpha(\beta)$ in equations 21 and 22 indicates that the site m(n) is occupied by atom of type $\alpha(\beta)$; the superscript e(p) refers to electron(positron) quantities. The integration in equation 22 is over the i^{th} cell volume Ω_i.

In general, Equations 18-22 are applicable to an arbitrary assembly of non-overlapping muffin-tin potentials. The central quantities which need to be evaluated for a given defect are the real space path operators T^e and T^p for the electrons and the positron via equation 20. We emphasize that the path operators need only be computed for the first few near neighbor shells of lattice vectors because the sum in equation 18 converges rapidly owing to the decaying nature of the trapped state positron wave function. We illustrate the theory by considering briefly the cases of a mono- and a di-vacancy in a perfect crystal.

The path operator for a mono-vacancy in an otherwise perfect crystal can be obtained by using the well known exact solution of the single impurity problem[8,11,40] (the "impurity" in this case being the vacant site) which involves the path operator for the perfect crystal and the phase shifts of the vacancy and the crystal muffin-tin potentials. For example, the (00) positron path operator is given by

$$T_v^{p,00}(E) = D_v(E)\, T^{p,c,00}(E), \tag{23}$$

where $T^{p,c,00}$ is the perfect crystal path operator, and

$$D_v(E) = [1 + (\tau_v^{-1}(E) - \tau_c^{-1}(E))\, T^{p,c,00}(E)]^{-1}. \tag{24}$$

Here, τ_v and τ_c refer to the positron muffin-tin potential for the vacant and the occupied crystalline sites respectively.

Various physically interesting quantities are obtained straightforwardly in terms of the path operators. For example, the bound state energy E_b for the vacancy-trapped positron is given by the poles of the path operator $T_v^{p,00}$ in equation 23. With equation 24 in mind, the relevant secular equation is[19]

$$\|[1 + (t_v^{-1}(E_b) - t_c^{-1}(E_b))T^{p,c,00}(E_b)]\| = 0. \tag{25}$$

Since the bound state positron will usually occupy an s-state, only the s-s element of equation 25 need normally be considered.

The charge on the vacant site is

$$\rho(\vec{r}) = -\pi^{-1} \int_{-\infty}^{E_F} dE\, Im\, G_v^{00}(\vec{r},\vec{r};E) \tag{26}$$

and the density of states is

$$\rho(E) = -\pi^{-1} \int_{\Omega} d^3r\, Im G_v^{00}(\vec{r},\vec{r};E), \tag{27}$$

where the mono-vacancy Green's function is given by equation 19 in terms of the path operator $T_v^{p,00}$. Equations 26 and 27 are applicable to either the positron or the electron.

We turn now to the case of a divacancy; here we must solve the "two impurity" problem, i.e., evaluate the divacancy path operators T_{div} in equation 20 when sites 0 and 1 are vacant and all others are occupied.[41] Note that if there are N sites and we include L_{max} angular momentum indices, equation 20 is of dimension $N \times L_{max}$; exact solutions are

however possible by matrix partitioning methods[42] for any element T^{nm}_{div}. For example, for $n = m = 0$

$$T^{00}_{div} = [T^{00} - T^{01} D_v a T^{10}] D_{div}, \tag{28}$$

where

$$a = \tau_0^{-1} - \tau^{-1}; \tag{29}$$

$$D_v = [a T^{00} + 1]^{-1} \tag{29}$$

and

$$D_{div} = [D_v^{-1} - a T^{01} D_v a T^{10}]^{-1}. \tag{30}$$

Here much of the notation is obvious; subscripts v and div denote mono- and di-vacancy quantities. Most important, equations 28-30 are only $L_{max} \times L_{max}$ matrices and express the defected medium path operators in terms of the medium path operators T^{00}, T^{01} and T^{10}. Expressions for path operators T^{nm}_{div} other than $n = m = 0$ can also be written down explicitly.

The approach outlined above for a divacancy is easily generalized to treat defects such as vacancy-impurity complexes. In these and other similar situations, we are faced with a problem where the defected region extends beyond the central site. The treatment of an M-atom "defect" placed in a medium is carried out (exactly) by a straightforward extension of equations 28-30; we will obtain in general an equation involving supermatrices of dimension $M \times L_{max}$ which are not difficult to handle for small M values.

Finally, in a disordered alloy, both sides of equation 18 are to be ensemble averaged; in a random binary alloy, we then obtain

$$< \rho_{2\gamma}(\vec{p}) > = \sum_{mn} < M_{mn}(\vec{p}) > \; e^{i\vec{p}\cdot(\vec{R}_m - \vec{R}_n)}, \tag{31}$$

where $< M >$, in view of equation 21, involves the configuration average $< Im T^e \; Im T^p >$ of the product of electron and positron path operators. Reference 19 proposes to first replace this average of products by a product of averages in the spirit of the IPM equation 10, followed by a further decoupling of the averages T^e_{mn} and T^p_{mn} in terms of KKR-CPA effective medium path operators, which are given by equation 20 with τ_i replaced by τ_{CPA} (see equation 6) on all lattice sites. Detailed formulae for $\rho_{2\gamma}(\vec{p})$ within this framework are presented in reference 19.

IIIB. Mono-vacancy in Cu

We discuss now results of reference 19 for a mono-vacancy in Cu on the basis of the KKR formalism of the preceding section . These are the first calculations of $\rho_{2\gamma}(\vec{p})$ for a vacancy trapped positron in a d-band metal based on a realistic muffin-tin potential. The previous work[43-45] on mono- and di-vacancy in Al, while establishing an important proof-of-principle, is based on pseudo-potential and super-cell approaches, which are difficult to extend to d-band systems and to disordered materials.

Figure 10 shows partially summed contributions $\rho_{2\gamma}^{(j)}(\vec{p})$ for a mono-vacancy in Cu ; the superscript (j) is to indicate that all contributions to $\rho_{2\gamma}(\vec{p})$ up to the j^{th} near neighbor shell in equation 18 have been included. It is striking that the $j = 0$ (vacant site) contribution is flat and featureless. In fact, the $j = 1$ curve, which adds contributions from the nearest neighbor (nn)-(110) shell to the $j = 0$ curve, leads to a dramatic change in shape; addition of contributions from subsequent shells yields relatively smaller changes. Figure 10 indicates that $\rho_{2\gamma}^{(1)}(\vec{p})$ is converged to within 10% of $\rho_{2\gamma}(\vec{p})$.

It is clear that the nn-(110)-shell and not the vacant site dominates the low p behavior of $\rho_{2\gamma}(\vec{p})$. This appears surprising because it may reasonably have been argued that , owing to the rapid decay of the trapped positron wave function with distance from the vacant site, all but the central site contribution will be negligible. The relative sizes of the vacancy and nn-shell terms can be understood by noting that $\rho_{2\gamma}(\vec{p})$ involves overlap of electron and positron wave functions. In the vacant site the positron amplitude is large but the electron density is quite small, while in the nn-shell a large electron charge density annihilates with the tails of the positron wave function. The exponential decay of the positron wave function will make the contributions from more distant cells much smaller. Our calculations show that about 48% of the positron charge resides on the vacant site in Cu. While this fraction can be expected to increase in cases of stronger positron vacancy binding energy, we expect the nn-shell contribution to dictate the shape of $\rho_{2\gamma}(\vec{p})$ curve in most metals.

Figure 11 compares $\rho_{2\gamma}(\vec{p})$ for the mono-vacancy along the three principal symmetry directions. $\rho_{2\gamma}(\vec{p})$ is less anisotropic for the trapped positron than for the Bloch-state positron; in particular, the latter contains pronounced FS breaks (see, for example, figure 4 or 5), which are not present in the trapped positron case. This result is expected, because the presence of the vacancy destroys translational symmetry of the system; the $\vec{k}$ conservation rules are relaxed, permitting all occupied electron states to contribute to $\rho_{2\gamma}(\vec{p})$.

Computations on alloys within the formalism of this section, together with high temperature 2D-ACAR measurements on Cu and CuGe are in progress. One important feature of the $\rho_{2\gamma}(\vec{p})$ may be anticipated in this connection. The fact that the low-$\vec{p}$ shape of $\rho_{2\gamma}(\vec{p})$ is controlled by the electronic structure in the nn-shell, suggests that the shape of the central peak in $\rho_{2\gamma}(\vec{p})$ will be a sensitive function of nn-shell composition. If so, 2D-ACAR experiments on vacancy-type defects may provide useful information about the nn-environment of the defects.

Several important effects not discussed so far need to be investigated in order to gain a satisfactory understanding of $\rho_{2\gamma}(\vec{p})$ for the vacancy trapped positron. These are the electron-positron correlations and the lattice relaxation[46] around the defected region. In connection with the electron-positron correlations, the "enhancement" effects on $\rho_{2\gamma}(\vec{p})$ have already been alluded to in the discussion of alloys in Section II above. Note further that the trapped positron (but not the Bloch-state positron) will attract additional electron charge in the vacant site; simple estimates indicate that a screening charge of about 0.3 electrons is drawn into the Cu mono-vacancy.[47]

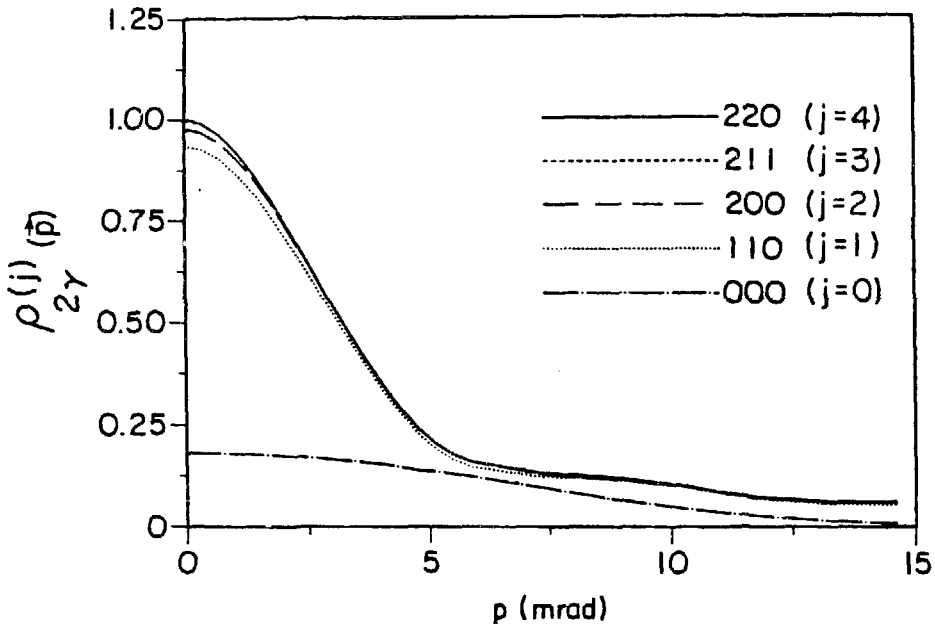

FIGURE 10: Partially summed momentum density $\rho_{2\gamma}^{(j)}(\vec{p})$ (see text) along [001] direction for various shells j.[After Ref. 19].

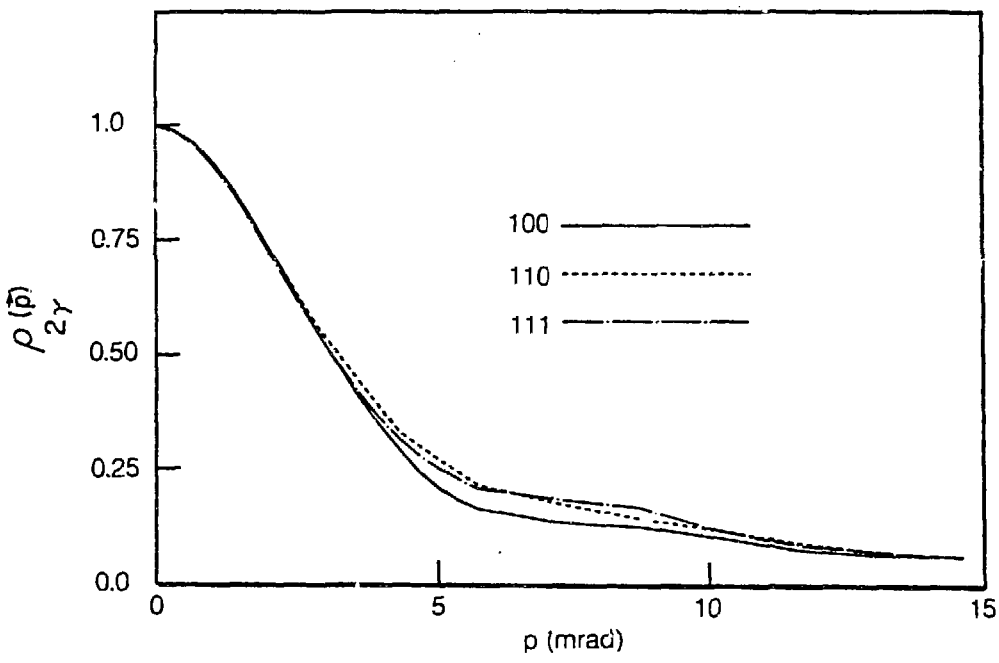

FIGURE 11: $\rho_{2\gamma}(\vec{p})$ for the vacancy trapped positron in Cu along principal symmetry directions.[After Ref. 19].

IV. STUDIES OF COMPOUNDS

Among compounds, high T_c ceramics, heavy Fermion alloys, Heusler alloys, and high-temperature aluminides are a few examples of systems of current interest. The application of the present theoretical framework or of the 2D-ACAR technique to such materials is in principle straightforward but faces difficulties of a more practical nature. On the experimental side, it is usually difficult to obtain good single crystals of reasonable size. Concerning theoretical methods, much of the momentum density work to date has involved simple close-packed non-magnetic metals and alloys of light atoms. In treating compounds of the type mentioned above, on the other hand, a substantially greater level of complexity cannot be avoided. For example, any meaningful discussion of heavy Fermion systems must include $f-$electrons and invoke a relativistic theory. Heusler alloys obviously cannot be considered in a non-magnetic framework. The lattices of many of the compounds are quite open, making it important to incorporate non-muffin-tin corrections to the potentials. Even in the case of an aluminide such as Ni_3Al where we have a close-packed metal with relatively light atoms, the $L1_2$ structure involves 4 atoms/unit cell, making any realistic $\rho_{2\gamma}(\vec{p})$ study computationally demanding. Finally, a satisfactory theory must obtain one-particle electron and positron potentials at some reasonable level of self-consistency. For these reasons, we should generally expect the calculations of $\rho_{2\gamma}(\vec{p})$ for compounds in the near future to be a "patchwork" of different techniques and approximations, dictated often by the computational resources and the specific aims in any given study. With these remarks in mind, we discuss briefly some of our own work in the area of compounds.

IVA. Heusler Alloys

Here we discuss the momentum density calculations of reference 48 on the $C1_b$ Heusler alloy $NiMnSb$. A striking feature of the spin-dependent band structure of this system is that the Fermi energy lies in a half-full majority spin band, but in a gap in the minority spin bands. The majority spin bands are thus metallic while the minority spin bands are semi-conducting.

Typical results for the majority spin momentum density $\rho^+_{2\gamma}(\vec{p})$ in $NiMnSb$ are presented in figure 12; figure 13 gives corresponding minority-spin results $\rho^-_{2\gamma}(\vec{p})$. The KKR scheme was employed for calculating these momentum densities, but the muffin-tin potentials were based on the self-consistent augmented spherical wave (ASW) computations of de Groot *et. al.*[49] In evaluating $\rho_{2\gamma}(\vec{p})$ by the KKR method angular momenta up to $l = 2$ were included in a scalar relativistic approximation.

In accord with its metallic nature, $\rho^+_{2\gamma}(\vec{p})$ in figure 12 shows several FS breaks, indicated by arrows. By comparing figures 12(a) and 12(b), we see that sizes and positions of the breaks vary with direction of $\vec{p}$ as is common in most metals. In contrast, the semi-conducting minority bands yield smooth $\rho^-_{2\gamma}(\vec{p})$ curves in figure 13. Interestingly, in figure 12 the dashed (unfilled) portion of the partial contribution from one of the bands exhibits a sharp dip at the Γ-point in the second BZ at $p = (0,0,2)$ and a corresponding peak at the Γ-point in the first BZ at $p = 0$. This feature is not related to FS breaks but is a

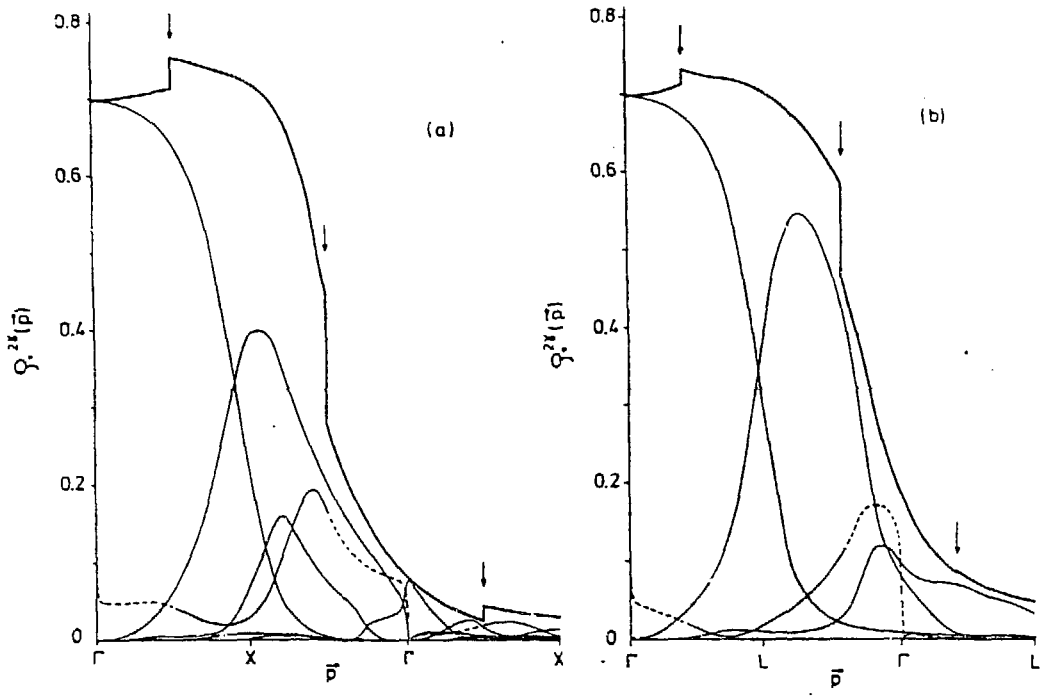

FIGURE 12: Momentum density $\rho^{+}_{2\gamma}(\vec{p})$ for the majority spin electrons in $NiMnSb$ (heavy solid). Thin lines give contributions to $\rho^{+}_{2\gamma}(\vec{p})$ from various bands; the dashed parts correspond to unoccupied states. The arrows indicate the positions of Fermi breaks. (a) and (b) refer to $\vec{p}$ along $\Gamma - X$ and $\Gamma - L$ directions respectively.

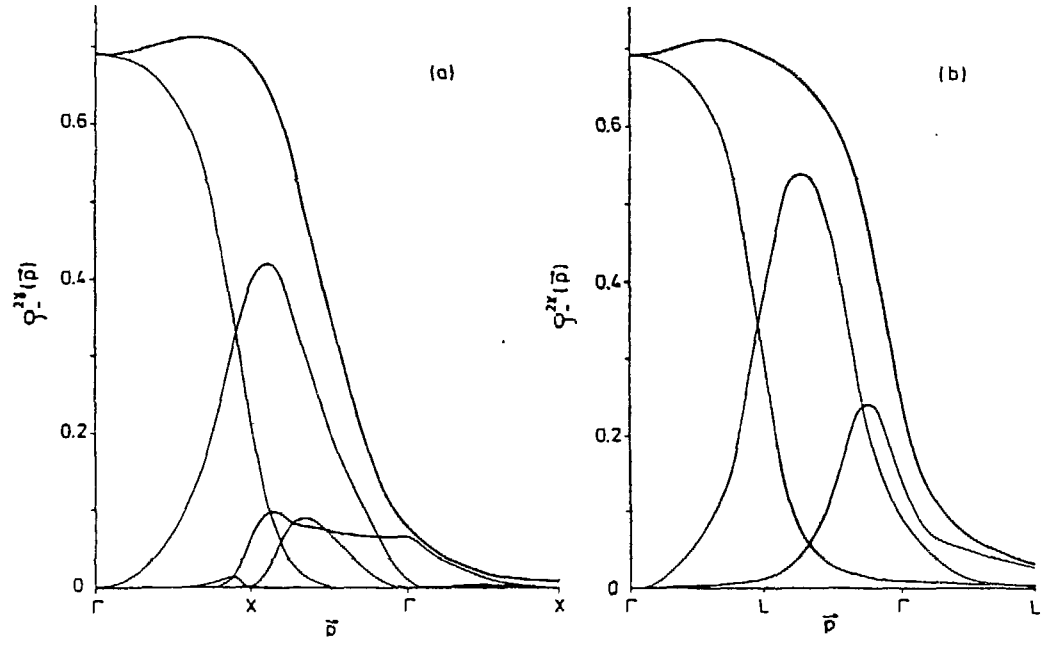

FIGURE 13: Same as the caption to figure 12, except that this figure refers to the minority spin density $\rho^{-}_{2\gamma}(\vec{p})$. [After Ref. 48].

rather subtle consequence of two bands of same symmetry hybridizing over a very small k-region around $\vec{k} = 0$. Since the portion of the band involved is unfilled, this effect cannot of course be observed in $NiMnSb$; in fact, more generally, if the Fermi energy lies either above or below the hybridizing bands, the total momentum density will not show any rapid variation.

It is clear that the majority and minority spin densities in $NiMnSb$ differ qualitatively. 2D-ACAR experiments on $NiMnSb$ single crystals are currently in progress. By carrying out two measurements in an external magnetic field which is parallel or anti-parallel to the positron polarization, it is possible to obtain individual contributions to the 2D-ACAR curves from the majority and minority bands separately. Ongoing comparisons of the measured spin-dependent distributions with calculations should offer insight into the electronic structure of the Heusler compounds.

IVB. Advanced Alloys: Ni_3Al

Ni and Fe $L1_2$ compounds with Al, Ga and Ge constitute important high-temperature alloys; over a substantial temperature range, these alloys become mechanically stronger with increasing temperature. They possess an unusual defect structure; for example, in Ni_3Al, anti-site defects occur for Al concentration less than 25%, and a small concentration of structural vacancies appears for more than 25% Al.[50,51] B doping increases the ductility considerably for alloys with less than 25% Al, but hardly affects alloys with more than 25% Al. Here, we discuss briefly 2D-ACAR results of reference 52 on Ni and Ni_3Al single crystals. The electronic structure and FS of Ni_3Al bears on the question of stability and magnetism of the $L1_2$ alloys more generally.[53-55]

A comparison of the cuts through the 2D-ACAR distribution along two typical directions in Ni and Ni_3Al in figure 14 (curves a and b) shows that the two set of data do not differ dramatically despite the change in lattice structure from fcc in Ni to $L1_2$-type in Ni_3Al. This is not surprising because the energy and momentum integrations in equation 2 and 13 reduce the sensitivity of the 2D-ACAR profiles to changes in lattice structure. The momentum density is more representative of the energy bands in an extended zone scheme, rather than the (usual) reduced zone energy bands.

Figure 14 explores the differences in Ni and Ni_3Al by decomposing the spectra into an isotropic (spherically symmetric; defined by curve c in each case) and the remaining anisotropic part, shown as curves e and f. [We will not comment on curve d in this brief discussion.] An inspection of the isotropic part c shows that the two spectra possess a different shape in the low $\vec{p}$ region. The anisotropic parts e and f, while displaying similarities, also show substantial differences. Many of the peaks in curves e and f, when reduced to the first BZ, map into the same $\vec{k}$-points, suggesting that the apparently random looking pattern of structures in these spectra contains useful FS information.

To enhance FS-induced features, the 2D-ACAR surface in $\vec{p}$-space was folded into the first BZ (an LCW-folding[56]) and once again decomposed into isotropic and anisotropic parts. Figure 15 shows a contour plot of the anisotropic contribution, together with a similar folding of the Ni data which would correspond to the hypothetical compound Ni_3Ni,

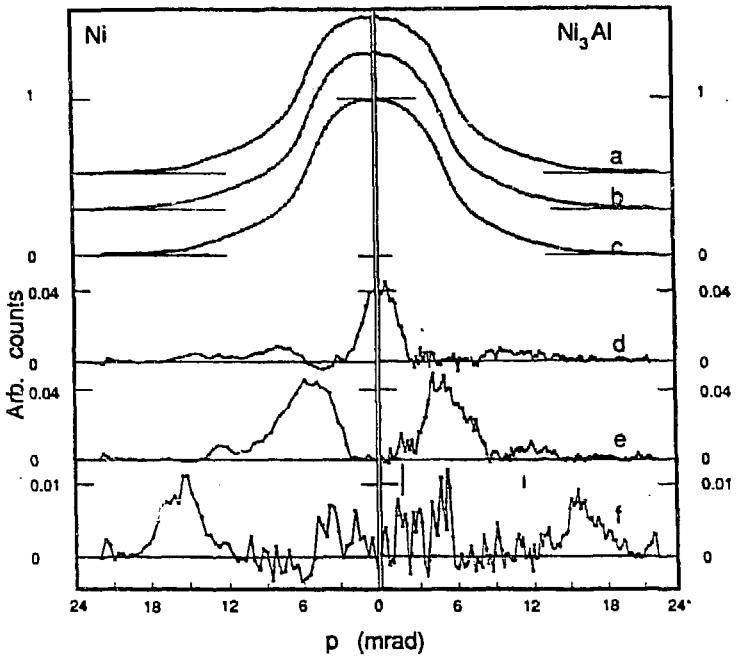

FIGURE 14: Results for Ni(left frame) and Ni_3Al (right frame). Upper part: cuts through the 2D-ACAR surface along [110] (curve a) and [100] (curve b); curve c gives the isotropic part in Ni and Ni_3Al. Lower part: curves e and f are the anisotropic parts of the spectra obtained by subtracting curve c from curves a and b respectively. Curve d gives anisotropic part along $[1\bar{1}0]$ starting at the symmetry point (R,M) in the Brillouin zone for hypothetical Ni_3Ni (see text), and Ni_3Al.

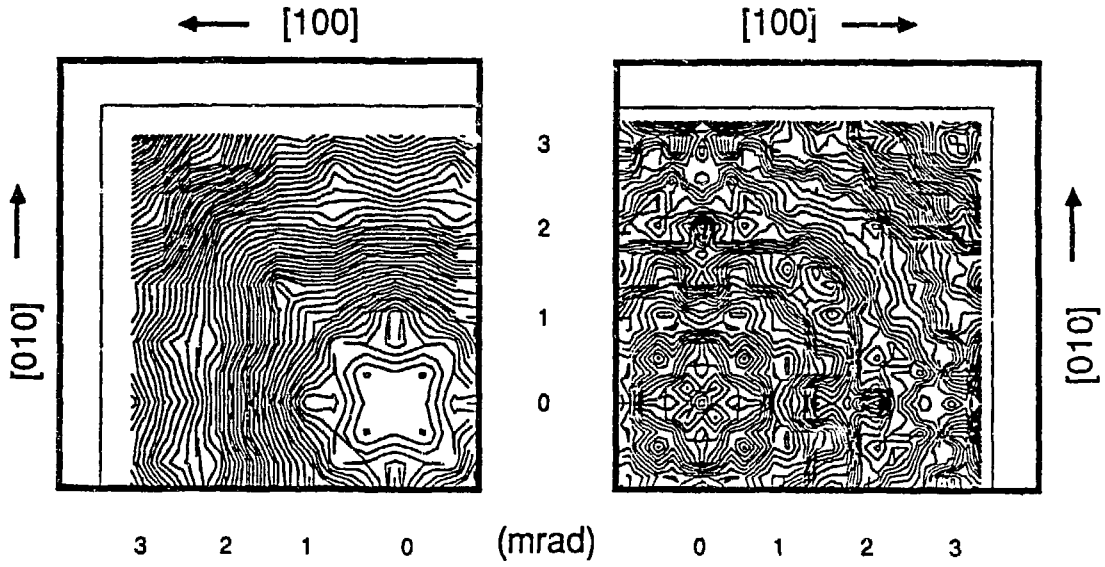

FIGURE 15: Contour plots of the anisotropic 2D-ACAR surfaces for hypothetical Ni_3Ni system (see text, left frame) and Ni_3Al (right frame) after folding the distribution in the first BZ.[After Ref. 52].

i.e., a system with the same crystal structure as Ni_3Al but with all the Al atoms replaced by Ni atoms. In such a representation, rapidly varying parts in the 2D-ACAR surface would be manifested as closely placed contours. A preponderance of such features is seen in Ni_3Al (right panel); this is to be generally expected because the FS of Ni_3Al possesses several electron and hole sheets. In comparing the measurements with theoretical FS predictions of Buiting *et. al.*[54], a substantial accord is found, including in particular a confirmation of the Γ_{16} sheet for the first time; see reference 52 for details. A theoretical study of the $\rho_{2\gamma}(\vec{p})$ and the associated 2D-distribution is necessary for a more general analysis of the the similarities and differences between the Ni and Ni_3Al 2D-ACAR measurements.

IVC. High T_c Ceramic Superconductors

The recent research activity concerning the high-T_c ceramics is perhaps the most intense ever undertaken by the scientific community at large. The original discovery of the $La-Sr-Cu$ compound with $T_c \approx 40K$ was rapidly followed by the $Y-Ba-Cu$ material with $T_c \approx 90K$, and the most recent reports of much higher T_c superconductors. The new materials are widely heralded as the beginning of a new era of technological applications and require little further general comment. One of the obvious challenges is to understand their electronic structure and its relationship to the unique properties of these materials. In this connection, we briefly discuss positron annihilation experiments of Smedskjaer *et. al.* on $YBa_2Cu_3O_{7-x}$.[57]

Positron annihilation Doppler broadening experiments were carried out as a function of temperature on $YBa_2Cu_3O_{7-x}$ polycrystals (pellets) with $x \approx 0.1$; the superconducting transition had a mid-point of $T_c = 92K$ with a width of 2K. The lineshape parameter S was obtained from measured spectra by integration over a 2.2 keV-broad region under the center of the distribution. S is seen from figure 16 to change abruptly at T_c and, furthermore, the temperature dependence of S on two sides of T_c is different. We summarize the main conclusions of reference 57, without presenting details. (*i*): the changes in S in figure 16 are mainly due to changes in the electronic structure as sampled by a positron in an extended Bloch-like state and not due to changes in positron trapping at defects. (*ii*): the behavior of S for $T < T_c$ can be accounted for in a simple BCS-like smearing of the electron momentum density if the presence of a heavy effective mass band is assumed close to the Fermi energy; this assumption is consistent with band structure calculations which show the presence of such a band arising from $Cu-O$ one-dimensional chains in $YBa_2Cu_3O_7$.[58] (*iii*): the discontinuity in S cannot be explained within the BCS-type theory and may indicate a change in band structure induced by the superconducting transition. While all explanations must necessarily be considered tentative at this stage of development, figure 16 indicates nevertheless that positron spectroscopy is sensitive to the superconducting transition in the high-T_c ceramics.

This work was supported by the U.S. Department of Energy, BES-Materials Science, under contracts DE-FG02-85ER45223 and W-31-109-Eng-38. It benefited from the allocation of supercomputer time on the ER-Cray at the MFE computer center.

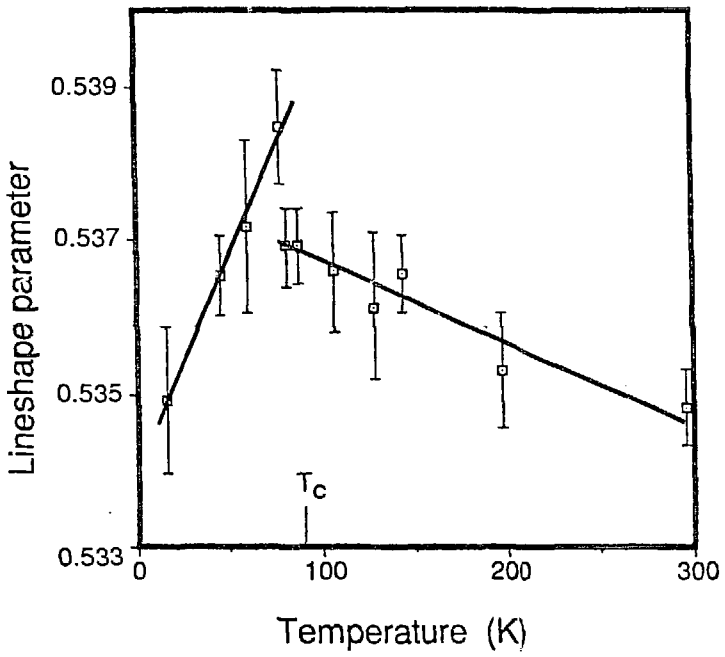

FIGURE 16: Doppler broadening lineshape parameter S for $YBa_2Cu_3O_{6.9}$ as a function of temperature. [After Ref. 57].

REFERENCES

1. S. Berko, in **Positron Solid State Physics**, edited by W. Brandt and A. Dupasquier (North-Holland, 1983).
2. A. P. Jeavons, Nucl. Instrum. and Methods **156**, 41(1978).
3. L. C. Smedskjaer and M. J. Fluss, in **Methods of Experimental Physics** (Academic, N. Y.., 1983), Vol. 21, p. 77.
4. P. Zwart, L. P. L. M. Rabou, G. J. Langedijk, A. P. Jeavons, A. P. Kaan, H. J. M. Akkerman, and P. E. Mijnarends, in **Positron Annihilation**, edited by P. C. Jain, R. M. Singru, and K. P. Gopinathan (World Scientific, Singapore, 1985), p. 297.
5. R. N. West, J. Mayers, and P. A. Walters, J. Phys. E. **14**, 478(1981). See also review by R. N. West in the volume in Ref. 4.
6. Y. Suzuki and M. Doyama, in the volume in Ref. 4.
7. H. Iriyama, I. Shinta, and S. Tanigawa, in **Positron Annihilation**, edited by P. G. Coleman, S. G. Sharma, and L. M. Diana (North-Holland, 1982), p. 895.

8. A. Bansil, in **Electronic Band Structure and its Applications**, Lecture Note Series, Vol. 283 (Springer-Verlag, Heidelberg, 1987), p. 273.

9. P. E. Mijnarends, Physica Status Solidi (1987).

10. A. Bansil in the volume in Ref. 7, p. 291.

11. G. M. Stocks and H. Winter, in **Electronic Structure of Complex Systems** (Plenum, 1984) p. 463.

12. P. E. Mijnarends, in the volume in Ref. 1.

13. see contribution by R. Prasad, and by R. S. Rao and M. Pessa in the volume in Ref. 8.

14. P. E. Mijnarends, L. P. L. M. Rabou, K. E. H. M. Hanssen, and A. Bansil, Phys. Rev. Letters **59**, 720(1987).

15. L. C. Smedskjaer, R. Benedek, R. W. Siegel, D. G. Legnini, and M. Stahulak, and A. Bansil (to be published).

16. R. M. Nieminen and M. J. Manninen, in **Positrons in Solids**, edited by P. Hautojarvi (Springer-Verlag, Heidelberg, 1979).

17. R. N. West in the volume in Ref. 16.

18. R. W. Siegel in the volume in Ref. 7, p. 351.

19. R. Prasad, R. Benedek, and A. Bansil in the volume cited in Ref. 4, p. 859; R. Prasad, R. Benedek, J. E. Robinson, and A. Bansil (to be published).

20. A. Bansil, R. S. Rao, P. E. Mijnarends, and L. Schwartz, Phys. Rev. **B23**, 3608(1981).

21. A. Bansil and M. Pessa, Physica Scripta **T4**, 52(1983).

22. A. Bansil and P. E. Mijnarends, Phys. Rev. **B30**, 628(1984).

23. P. E. Mijnarends and R. M. Singru, Phys. Rev. **B19**, 6038(1979).

24. T. Jarlborg, A. K. Singh, Phys. Rev. B(1987).

25. B. Chakraborty, Phys. Rev. **B24**, 7423(1981). See also review by Chakraborty in the volume in Ref. 7.

26. E. Boronski, R. M. Nieminen, and L. J. Lantto, Phys. Rev. **B32**, 1377(1985).

27. See review by J. Arponen and E. Pajanne, in the volume in Ref. 4.

28. R. Benedek, R. Prasad, S. Manninen, B. K. Sharma, A. Bansil, and P. E. Mijnarends, Phys. Rev. **B32**, 7650(1985).

29. A. Bansil, Sol. State Commun. **16**, 885(1975).

30. R. Prasad and A. Bansil, Phys. Rev. Letters **48**, 113(1982).

31. M. R. Halse, Philos. Trans. R. Soc. London, Ser. A. **265**, 507(1969).

32. B. L. Gyorffy and G. M. Stocks, Phys. Rev. Letters **50**, 374(1983).

33. R. S. Rao, A. Bansil, H. Asonen, and M. Pessa, Phy. Rev. **B29**, 1713(1984).

34. Z. Szotek, B. L. Gyorffy, G. M. Stocks, and W. M. Temmerman, J. Phys. **F14**, 2571(1984).

35. K. Ohshima and D. Watanabe, Acta. Crys. **A29**, 520(1973).

36. K. Ohshima, D. Watanabe, and J. Harada, Acta. Crys. **A32**, 883(1976).

37. M. Hasegawa, T. Suzuki, and M. Hirabayashi, J. Phys. Soc. Japan **43**, 89(1977).

38. Appendix of Ref. 20

39. J. S. Faulkner and G. M. Stocks, Phys. Rev. **B21**, 3222(1980).

40. H. Ehrenreich and L. Schwartz, Sol. State Phys. **31**, 149(1976).

41. R. Prasad, A. Bansil, and R. Benedek (to be published).

42. A. Gonis, G. M. Stocks, W. H. Butler and H. Winter, Phys. Rev.**B29** 555(1984).

43. R. P. Gupta and R. W. Siegel, Phys. Rev. Letters **39**, 1212(1977); Phys. Rev. **B22**, 4572(1980).

44. B. Chakraborty and R. W. Siegel, Phys. Rev. **B27**, 4535(1983).

45. M.J. Fluss, S. Berko, B. Chakraborty, K.R. Hoffman, P Lippel and R.W. Siegel, J. Phys. F **14**, 2831 (1984); M.J. Fluss, S. Berko, B. Chakraborty, P. Lippel and R.W. Siegel, J. Phys. F **14**, 2855 (1984).

46. N. Stefanou, P. J. Braspenning, R. Zeller, and P. H. Dederichs, Phys. Rev. **B36** (1987).

47. J.E. Robinson, R. Benedek and R. Prasad, Phys. Rev. **B35**, 7392(1987).

48. K. E. H. M. Hanssen and P. E. Mijnarends, J. Phys. F. (1987).

49. R. A. de Groot, F. M. Mueller, P. G. van Engen, and K. H. J. Buschow, Phys. Rev. Letters **50**, 2024(1983).

50. M. Shimotomai, T.M. Wang, T. Iwata and M. Doyama, p140 in volume in Ref. 4.

51. A. Dasgupta, L. Smedskjaer, Legnini and R.W. Siegel, Materials Letters **3**, 457 (1985).

52. L. C. Smedskjaer, A. DasGupta, D. G. Legnini, and M. D. Stahulak (to be published).

53. See, for example, C.R. Bull, R.N. West, N. Kawamiya, and N. Shiotani in the volume in Ref. 4.

54. J. Buiting, J. Kübler, F.M. Muller, J. Phys. F **13**, Kübler L179 (1983).

55. T. Moriya, J. Magn. Mag. Mat. **14**, 1 (1979).

56. D. G. Lock, V. H. C. Crisp, and R. N. West, J. Phys. **F3**, 561(1973).

57. L. C. Smedskjaer, B. W. Veal, D. G. Legnini, A. P. Paulikas, and L. J. Nowicki (to be published).

58. S. Massida, J. Yu, A. J. Freeman, and D. D. Koelling, (to be published); W. Y. Ching, Y. Xu, G. Zhao, K. W. Wong, and F. Zandiehnadem (to be published).